Large-bore copper-vapor lasers: Kinetics and scaling issues[a)]

M. J. Kushner and B. E. Warner
Lawrence Livermore National Laboratory, University of California, Livermore, California 94550

(Received 17 January 1983; accepted for publication 8 March 1983)

The scaling characteristics of large diameter ($6 \leqslant d \leqslant 12$ cm) high repetition-rate copper-vapor lasers are investigated using a radially dependent laser-discharge model. Results of the model are verified with experimental data obtained on several devices including an 8-cm-diam 100-W copper-vapor laser. Two effects, penetration of the applied electric field into the plasma and gas heating, which we show are the primary considerations in volumetric scaling, are discussed in detail. Thermal constriction of the discharge resulting from gas heating is prevented by plasma skin effects that allow stable performance at large diameters. These same effects are shown to explain the sequential excitation of the laser levels, resulting in both temporally and spatially dependent behavior of the laser pulse. Projections of output power and light-pulse characteristics are made for lasers up to 12 cm in diameter.

PACS numbers: 42.55.Hq, 52.80.Hc, 52.25.Lp, 42.60.By

I. INTRODUCTION

The copper-vapor laser (CVL) is one of a number of electric-discharge-excited metal-vapor lasers that are characterized by laser transitions from an excited state to a low-lying metastable state.[1] These self-terminating lasers typically produce light pulses that are tens of nanoseconds long at visible wavelengths. Copper lasers, which have green (510.6 nm) and yellow (578.2 nm) transitions, are distinctive because of their rather high electrical efficiency ($\approx 1\%$) and because they have been scaled to high average power operation (> 100 W).

Since the first demonstration of the CVL in 1966,[1] laser oscillator power has been increased from 20 mW at 660 Hz in a 1-cm-diam tube to more than 100 W at 5 kHz in an 8-cm-diam tube.[2–6] This improvement in performance is due primarily to increasing the laser repetition rate, greater sophistication in the discharge circuitry and thermomechanical design, and from volumetric scaling of the discharge region. Volumetric scaling can be accomplished by lengthening the discharge or increasing its diameter. Length scaling is straightforward but rapidly reaches the limits of present high-voltage pulsed power technology. However, the most important step for increasing laser power was increasing the diameter of the discharge tube. Early in the development of the CVL it was assumed that the metastable lower laser level was relaxed by diffusion to and subsequent deactivation by the walls of the discharge tube. Long diffusion times implied that there was a limited regime of pressure and diameter for efficient operation at high repetition rates. The realization that, under suitable conditions, the lower laser level could be deactivated instead, by collisions with electrons in the plasma, led to the present generation of large-diameter devices that are actually limited in specific output power by gas heating rather than diffusion.

Under this assumption a number of studies[7–11] were performed to verify scalability in the radial direction for lasers using pure metallic sources. Unfortunately, the results of this work, made on lasers less than 4 cm in diameter, do indeed indicate that even with volumetric deactivation, excessive heating of the center of the discharge still seriously limits the ultimate useable discharge-tube diameter by thermally populating the metastable lower laser level. The present investigation was undertaken to clarify this issue and to explore effects particular to large-bore high-repetition-rate discharges. The experimental work presented in this paper is based on CVLs, as large as 8 cm diameter, having a maximum output of 100 W at a repetition frequency of 5 kHz. A detailed spatially dependent kinetic model is presented and its results are compared with experimental results. We limit the discussion to CVLs with diameters greater than or equal to 6 cm. It is at this diameter we have found that computer predictions based on "zero-dimensional" modeling[12] begin to seriously deviate from experimental results. The primary source of this deviation is due to the plasma skin-depth phenomenon which is manifested by a radial and temporal variation of laser excitation. We have found it necessary to spatially model the CVL kinetics, including plasma skin effects, to obtain accurate predictions for lasers greater than 6 cm diameter.

In Sec. II, we begin with a description of the kinetic model called CuRAD. The results of the calculations are then displayed covering the parameter ranges of interest for high-repetition-rate lasers. In Sec. III we show the basis for the important model assumptions, which is derived from hook spectroscopy and laser-performance measurements obtained from 6-, 7-, and 8-cm-diam lasers in our laboratory. Finally, we present scaling predictions to even larger-diameter devices based on the code and experimental work. In Appendixes A and B, relatively simple models are discussed, which allow us to bound the magnitudes of the gas heating and skin-depth phenomena and also provide physical insight into the nature of these effects.

II. DESCRIPTION OF THE MODEL

The CVL, like other discharge-excited lasers, depends critically on external circuit and thermodynamic parameters

[a)] Work performed under the auspices of the U.S. Department of Energy by the Lawrence Livermore National Laboratory under Contract No. W-7405-ENG-48.

 0021-8979/83/062970-13$02.40

to an extent that an accurate model must include energy deposition, circuit performance, kinetics, and state variables in a well-coupled self-consistent manner. Furthermore, achievement of a quasisteady state of the thermodynamic parameters and species populations requires that many discharge pulse and afterflow cycles be sequentially calculated for accurate results.

The model presented here is based on a "zero-dimensional" model[12] that integrated the coupled set of differential equations over several discharge cycles. This simpler zero-dimensional model has proven to be reasonably accurate for predicting the performance of small-bore CVLs up to 5–6 cm in diameter, but then details of the light pulse become inaccurate. The major revisions in the previously described model are (a) the addition of the $4P\,^2P_{1/2}$ and $4S\,^2D_{3/2}$ states in copper to include the yellow 578.2-nm laser transition, (b) revision of certain excitation cross sections, (c) a change in the buffer gas from helium to neon, and (d) inclusion of explicit radial dependence of the kinetic and thermodynamic variables used in the model. This last feature is the key to developing a mathematical description of this laser, which allows us to extrapolate to larger-diameter lasers.

Our laboratory devices are usually operated at about 5 kHz with neon as the buffer gas at about 30-Torr pressure. Unless noted otherwise, the computed results discussed here have been optimized with respect to copper density. This density, typically 10^{14}–$10^{15}/\text{cm}^3$, is a function of the temperature of the discharge tube, where the copper sources are placed. The discussions below are for lasers with these parameters. For a detailed discussion of the effect of varying buffer-gas pressure, tube temperature, and repetition rate, see Ref. 12. When laser power is discussed, we are referring to the sum of the power from the yellow and green transitions.

We begin the description of the model by defining the species whose populations will be calculated as a function of space and time.[13] Figure 1 shows the energy levels of copper and the buffer gas, which in this case is neon. Seven levels for the copper atom and four levels of the neon buffer gas are used. The copper levels are the $^2S_{1/2}$ ground state, $^2D_{5/2}$ and $^2D_{3/2}$ metastable states (lower laser levels), $^2P_{1/2}$ and $^2P_{3/2}$ (upper laser levels), a pseudostate, and the copper ground-state ion. The 578.2-nm (yellow) laser transition is between the $^2P_{1/2}$ and $^2D_{3/2}$ states and the 510.6-nm (green) laser transition is between the $^2P_{3/2}$ and $^2D_{5/2}$ states. Under optimum operating conditions, the ratio of green-laser to yellow-laser power is found to be approximately 2 to 1, which is the ratio of the statistical weights of the upper laser levels. The pseudostate is an average of higher lying levels and displaced terms.[14] These neutral atomic states and the copper ion were found sufficient to model accurately the laser while keeping the number of states to a minimum to make the problem computationally tractable. The buffer-gas states were chosen in a similar manner.

For cross sections between excited copper states we used the computed results of Henry.[14,15] Cross sections for the excitation of the laser levels from the ground state were taken from Refs. 15 and 16, renormalized by Winter and Hazi.[17] The cross section for the ionization of the copper

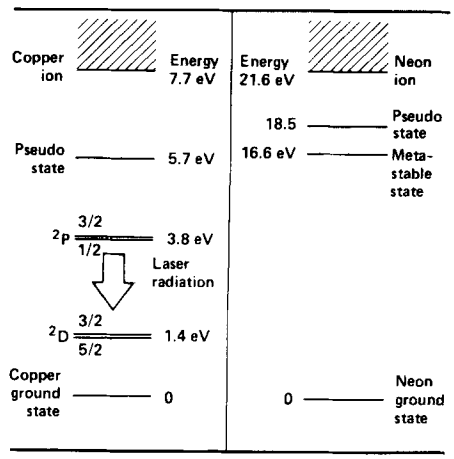

FIG. 1. Atomic species included in the model and energy level diagrams. (Note the change in vertical scales.)

ground state came from a calculation by Rescigno.[18] Figure 2 summarizes the low-energy excitation rates for the copper transitions used in CuRAD. These rates were calculated by averaging the cross sections listed above over a Maxwellian electron distribution with temperature T_e (see discussion below). Excitation cross sections for the neon buffer gas were taken from the compilation by Kieffer.[19]

In the next two subsections we discuss the six equations which form the basis of CuRAD. They are broken up into two groups. Section A includes the electric field, electron temperature, and electron density equations. Section B describes the particle density and gas temperature equations. The electric field and electron equations form the driving part of the laser model. The particle density and gas temperature equations can be thought of as reacting to this discharge drive.

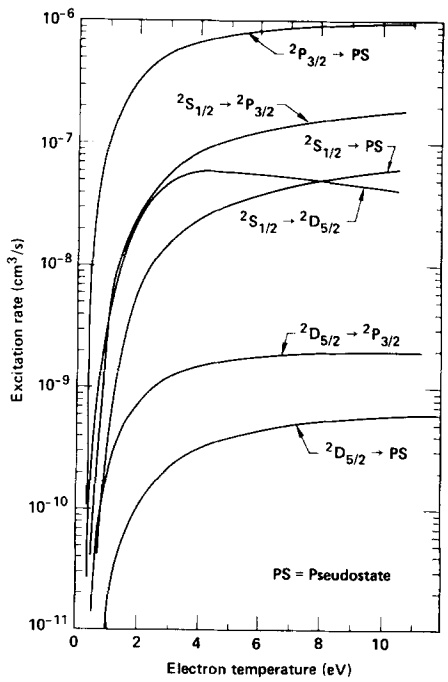

FIG. 2. Copper electron impact excitation rates used in CuRAD.

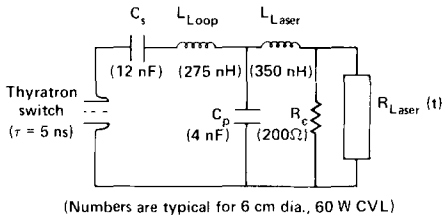

FIG. 3. Laser discharge circuit.

A. Electric field, electron temperature, and density equations

Energy flows from the electrical drive circuit to the laser by heating the electrons left over from the previous discharge pulse. These collide with the copper and neon atoms, creating the desired population inversion and ultimately heating the gas in the discharge. Subsequent cooling of the gas by conduction to the walls heats the discharge tube to the correct operating temperature to maintain the optimum copper-vapor density. We assume only a longitudinal electric field is applied. Circuit effects determine the net applied electric field external to the laser. To maintain self-consistency, we include a detailed circuit model.[12] Figure 3 shows the basic modulator circuit. The electric field in the discharge is self-consistently determined by the circuitry, electron temperature, and electron density. It is included as a radial and temporal variable in the system of equations by Maxwell's equations in their vector form. The resultant longitudinal electric field is described by a diffusion-like equation:

$$\nabla^2 E = \mu_0 \frac{\partial}{\partial t}(\sigma E)\,. \tag{1}$$

Because it is difficult to see skin effects explicitly outside the computational formalism, we refer the interested reader to Appendix A where a simple one-dimensional treatment motivates a physical understanding of this important effect.

The electron energy distribution is assumed to be Maxwellian, described by a temperature T_e. The use of a Maxwellian electron distribution was necessitated by the prohibitive computing time required to solve Boltzmann's equation explicitly. By using a Maxwellian distribution, excitation rates for levels with high excitation energies are likely to be overestimated.[20] In a copper–neon discharge having an average electron temperatures between 1 and 5 eV, this discrepancy is small for the copper excitation rates. We have verified this by solving Boltzmann's equation for the electron distribution under typical conditions for our lasers. However, the use of a Maxwellian may overestimate the rates for excitation of the neon levels. The fraction of discharge energy that is deposited in the neon excited states and neon ion is sufficiently small that even if overestimated, has a relatively small influence on the laser kinetics.

The equation used to solve for the electron temperature is

$$\frac{\partial}{\partial t}\left(\frac{3}{2} n_e k T_e\right) = \frac{n_e e^2 E^2}{m \nu_m} - \sum_{i,j} r_{ij} N_i n_e \epsilon_{ij} + \sum_{i,j} r^s_{ij} N_i n_e \epsilon^s_{ij} + \sum_i N_m N_i r_p \epsilon^p_i - \sum_i \frac{3}{2} n_e k \left(\frac{2m}{M_i}\right) \times (T_e - T_g)\nu^i_m + \nabla \cdot \left(u \frac{3}{2} n_e k T_e\right) + \nabla \cdot (\lambda_e \nabla T_e)\,, \tag{2}$$

where all of the variables are radially dependent. In Eq. (2), n_e is the electron density, r a rate constant, ν_m the electron momentum-transfer collision frequency, E the longitudinal electric field, T_g the gas temperature, ϵ energy lost or gained by electrons, m the electron mass, and M_i the mass of a heavy particle (copper or neon). During the discharge pulse the first three terms are dominant. The remaining terms dominate during the afterglow. The first term of Eq. (2) is for energy gained from the longitudinal electric field, the second term is for energy loss ϵ_{ij} as a result of the jth inelastic collision with species i, and the third term is the analogous increase in energy due to superelastic collisions. The fourth and fifth terms in Eq. (2) account for the energy gained as a result of Penning ionizations and energy exchange with gas atoms and ions due to elastic collisions. The sixth term of Eq. (2) is for the change in electron temperature as a result of convection. The last term in Eq. (2) is the change in electron temperature resulting from conduction. Electron transport in the radial direction is assumed to be limited by ambipolar diffusion, so the convective velocity u is given by

$$u = \mu_e E_r - D_e \nabla n_e / n_e\,, \tag{3}$$

where μ_e is the electron mobility, E_r the radial electric field, and D_e the electron diffusion coefficient. The radial ambipolar electric field is[21]

$$E_r = \frac{-D_e \nabla n_e + \sum_i D^i_I n^i_I}{\mu_e n_e + \sum_i \mu^i_I n^i_I}\,. \tag{4}$$

In Eq. (4) the sums are over the ionic species.

Late in the afterglow, the last term of Eq. (2), the conductive heat flux, is most influential in determining the radial profile of the electron temperature over the cross section of the discharge. This results from the high electron density ($> 10^{13}/\text{cm}^3$) and consequently large thermal conductivity[21] that decouples the electron gas from explicit dependence on the local gas temperature. That is, perturbations in the local electron temperature by collisions with the gas atoms are quickly distributed throughout the electron gas. The end result is that the electron temperature is fairly uniform across the diameter of the discharge tube beginning tens of microseconds after the discharge pulse and continuing during the remainder of the afterglow.

At the surface of the dielectric discharge tube, a plasma sheath forms. Since the plasma potential of the afterglow is very likely to be positive, electrons will be excluded from a region a few Debye lengths thick adjacent to the wall. Because the electron thermal conductivity is proportional to the electron density, this region would act as a layer of insulation with respect to conductive heat transfer to the wall by electrons. As a result of this argument, we have chosen the

boundary condition at the wall such that there is negligible electronic conductive heat transfer across it.

The governing equation for the electron density is

$$\frac{\partial n_e}{\partial t} = \sum_i r_i^I n_e N_i - \sum_i N_i^I n_e (r_r + n_e r_{crr}) + \sum_i N_m N_i r_p - \nabla\cdot(u n_e) . \quad (5)$$

In Eq. (5) the terms are for ionization of species i with rate r_i^I, radiative recombination with ion i with rate r_r, collisional radiative recombination with ion i with rate r_{crr}, Penning ionization of species i with rate r_p, and convective transport of electrons with velocity u. Extending the plasma-sheath argument, we choose the boundary condition to be $n_e = 0$ at the wall. In Eq. (5) the first term dominates during the discharge pulse and the remaining terms dominate during the afterglow.

B. Particle density and gas temperature equations

The local density of excited species is determined primarily by the local electron–atom collision rates. This is because diffusion is very slow at these relatively high pressure discharges, e.g., the diffusion loss rate for neutral species is about 50/s, so during one discharge cycle (200 μs at kHz) the loss of excited-state atoms by diffusion accounts for less than 1% of the total change in density. The time rate of change in density of neutral species i is given by

$$\frac{\partial N_i}{\partial t} = \sum_j (r_e^{ji} N_j - r_e^{ij} N_i) n_e + \sum_{j,k} r_H^{kji} N_j N_k - \sum_{j,k} r_H^{kij} N_i N_k + \nabla\cdot D_i \nabla N_i - \nabla\cdot(u_N N_i) + \frac{N_i}{P}\frac{dP}{dt} . \quad (6)$$

In Eq. (6) r_e^{ji} is the rate for electron-impact excitation between species j and i. The analogous rate for excitation between species j and i by collision with heavy body k is r_H^{kji}. The diffusion constant for species N_i is D_i and the neutral species convective velocity u_N. The last term accounts for changes in density due to relaxation of the radially averaged gas pressure to the reservoir value exterior to the heated region. Under the conditions of constant number density the convective velocity is given by

$$\sum_i \nabla\cdot(u_N N_i) = \sum_i \frac{N_i}{T_g}\frac{\partial T_g}{\partial t} - \frac{1}{A}\int_0^R \times \sum_i N_i \frac{1}{T_g}\frac{\partial T_g}{\partial t} 2\pi r dr , \quad (7)$$

where the integral in Eq. (7) ensures that the number of particles is conserved.

The gas (neon and copper vapor) temperature, which controls most of the macroscopic behavior of large-diameter copper lasers, is an important parameter in our laser-discharge model. However, the detailed kinetic influences of the gas temperature are numerous and complicated. The expression we use to describe the time rate of change in the gas temperature is given by

$$\frac{\partial}{\partial t}\left(\frac{3}{2} N k T_g\right) = J E_L + \sum_j \frac{3}{2} n_e k \frac{2m_e}{M_j} \times (T_e - T_g)\nu_m^j + \nabla\cdot\lambda_g \nabla T_g . \quad (8)$$

In Eq. (8), E_L is the local longitudinal electric field, J the local current density, M_j the mass species j, ν_m^j the collision frequency of electrons with species j, and λ_g the temperature-dependent gas thermal conductivity. The first term JE_L is the Joule heating of the gas due to current flow through it. The local gas heating due to this term can vary greatly across the diameter of the discharge, depending on the energy-deposition profile, i.e., the local longitudinal electric field. The second term of the rhs of Eq. (8) is a heating term due to collisions with electrons during the afterglow. The analogous term in Eq. (2) cools the electrons. In this manner during the afterglow the gas temperature couples to the electron temperature and consequently to the deexcitation rates of neutral species. As will be discussed, this is the mechanism by which the gas temperature plays a critical role in determining the population density of the copper metastable lower laser levels just prior to the discharge pulse. The third term in Eq. (8) is for conduction to the discharge walls. Coupled with the heating terms, this conduction term requires that the gas at the center of the discharge be hotter than that at the walls. (We assume the gas temperature is equal to the wall temperature at the wall.) Since conduction is the only heat-loss process for the gas, varying laser diameter and power loading can have large effects on the average gas temperature and radial temperature profiles.

III. DISCUSSION OF THE MODEL RESULTS AND COMPARISON WITH EXPERIMENT

In this section, code predictions are compared with data from 6 to 8-cm-diam CVLs to demonstrate typical kinetic behavior and to verify the accuracy of the code on several different laser diameters. The data are obtained from two sources: time-resolved copper excited-state population densities for 8-cm-diam CVLs[22,23] obtained with hook spectroscopy,[24,25] and output power parameterization for 6-, 7-, and 8-cm-diam CVLs, which has been gathered over the past several years in our laboratory.[26] The hook spectroscopy data have a systematic uncertainty of $\pm$ 20% resulting from uncertainties in the length of the heated region (which is less than the electrode separation) and the oscillator strengths of the transitions. In addition, there is a $\pm$ 5% random error resulting from timing jitter in the probe laser and the finite resolution available with the data-reduction technique. Due to uncertainties in the cross sections and rate constants used in the model, the computed results have a systematic uncertainty of about $\pm$ 20%. The experimental data, as well as the model predictions, will be discussed for lasers operating at 5 kHz. This value was chosen since average laser power under our operating conditions is maximum in the 4–6-kHz range.

A. Axial behavior

We begin by examining the laser along its central axis ($r = 0$). There are two time domains that interest us in the

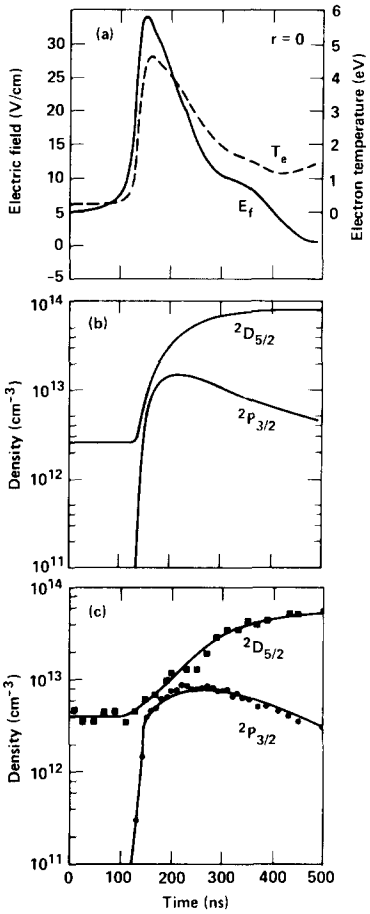

FIG. 4. (a) Calculated electric field and electron temperature, 8-cm laser, $r = 0$; (b) calculated green laser level populations; (c) hook diagnostic measurement of green laser level populations.

detailed kinetics of the copper laser: the discharge pump pulse, which lasts for approximately 500 ns and the afterglow, which lasts for the next 200 μs. Plotted in Fig. 4 are code predictions for various kinetic parameters during the pump pulse of the CVL. In Fig. 4(a) the longitudinal electric field and the resultant electron temperature are plotted as a function of time. Approximately 150 ns after switch closure ($t = 0$) the electric field in the plasma reaches a maximum value of 30 V/cm and the electron temperature is calculated to be about 4.5 eV. As the electric field diminishes, the electron temperature decays quickly. In Fig. 4(b) the predicted laser level populations for the two transitions involved in the green light output are plotted. Notice the metastable $^2D_{5/2}$ level is populated from the previous discharge pulse to a value of $\approx 3\times 10^{12}$ cm^{-3}. When the discharge pulse starts, the electron temperature increases and the $^2D_{5/2}$ level increases in density to the high 10^{13} cm^{-3}. The upper laser level population $^2P_{3/2}$ increases simultaneously with the rise in the $^2D_{5/2}$ population. Notice that the density of atoms in the $^2P_{3/2}$ state does not exceed the density of atoms in the $^2D_{5/2}$ state. The inversion is partial, a result of the favorable difference in statistical weights of the two levels. Shortly after the electric field has decreased to near zero, the $^2P_{3/2}$ level decays due to radiation and electron impact deexcitation. The $^2D_{5/2}$ metastable level slowly peaks due to continued electron impact excitation from the ground state.

Plotted in Fig. 4(c) are the hook diagnostic measurements for the $^2D_{5/2}$ and the $^2P_{3/2}$ states. The direct population measurements are in good agreement with the code predictions. The measured prepulse density is $\sim 4\times 10^{12}$ cm^{-3} and peaks to within 30% of the same level as predicted by the code. The copper levels involved with the yellow laser transition show behavior similar to the green transition, with the exception that the yellow metastable population has a lower value at the beginning of the discharge pulse. This is a result of its higher excitation energy and therefore lower thermal equilibrium density.

The afterglow time regime is also important for the CVL because it sets the initial conditions of the discharge for the next pumping pulse. Displayed in Fig. 5(a) and 5(b) are code predictions for the $^2D_{5/2}$ density and the electron temperature during this period. Note that the $^2D_{5/2}$ density asymptotically relaxes to its equilibrium value during the afterglow. This value of about $3\text{–}4\times 10^{12}$ cm^{-3} results from the detailed balance between the electron temperature, the copper ground state and its metastable level. As seen in Fig. 5(b) the electron temperature decays to the gas temperature. It is important to understand that the average gas temperature is the lower limit to which the electron temperature can decay.

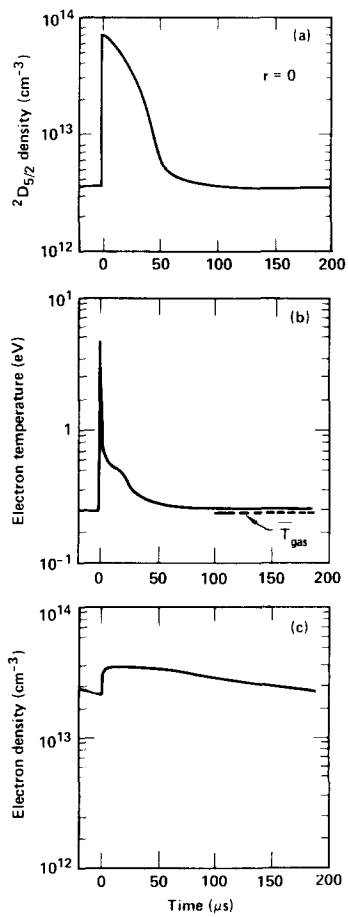

FIG. 5. (a) CuRAD prediction of metastable density in the afterglow; (b) electron temperature decay in afterglow; (c) electron density in afterglow.

As we see in Fig. 5(c) the predicted electron density during the afterglow does not vary by more than a factor of 2 or 3. This is a consequence of two effects: first, the loss of electrons by ambipolar diffusion is extremely slow due to the large discharge tube diameter and relatively high pressure of the neon buffer gas; second, since the electron temperature remains greater than 0.3 eV until the very end of the afterglow period, the recombination rate remains small. (Recall that collision radiative recombination is proportional to $T_e^{-4.5}$.)

Data have been gathered in our laboratory over the last few years on 6-, 7-, and 8-cm-diam CVLs. Nominal operating characteristics for these lasers, as well as code predictions for laser output power and laser pulse length, are listed in Table I. Typically the distance between electrodes is 120–150 cm while the heated region is about 30 cm shorter. The operating temperature ($\approx$1450 °C) yields a copper partial pressure of about 0.15 Torr in a neon buffer-gas pressure of 25–30 Torr. As indicated in Table I, we have found that as the laser is scaled to larger diameters, the optimum charging voltage increases while the input discharge power density decreases. This issue will be addressed in detail in Sec. IV. The agreement between the experiment and code predictions for laser output power and laser pulse length is quite good, being within 10%–15% in all cases, and gives us confidence in using the model to predict laser characteristics for devices greater than 8 cm diameter.

B. Gas temperature effects

The above discussion points out the influence of gas temperature on electron temperature in the afterglow, emphasizing the strong coupling between afterglow electron temperature and laser inversion density during the succeeding laser pulses. Gas-temperature effects such as this in small-diameter and transverse CVLs have been discussed in the literature.[27,28] These effects, however, become more important in large-diameter lasers and therefore warrant further discussion. In this section we digress to describe the nature of gas heating in high repetition-rate CVLs and its influence in large-diameter lasers.

During a single pulse of the CVL, approximately 0.1–1 J of energy is deposited in the gas. The corresponding single-pulse increase in gas temperature, however, is not large for typical CVLs. It can be estimated from the specific heat of the buffer gas c_p

$$\Delta T = \frac{\Delta Q}{\rho c_p}, \tag{9}$$

where ρ is the molar density. The incremental increase in gas temperature is ΔT and ΔQ is the energy input per pulse. For an 8-cm laser operating at 30 Torr neon and 1.2 J/pulse into the discharge, the temperature rise is $\Delta T = 150$ °C, which is small compared to the average gas temperature of several thousand degrees. This single-pulse temperature rise does not significantly influence the kinetics of the laser. Note that the low partial pressure of copper (0.1 Torr) means that it contributes little to the heat capacity.

With our 8-cm CVL operating at typically 5 kHz, nearly 6 kW of average power are deposited in the gas. The dominant heat-loss mechanism is conduction to the walls, while heat deposition is a volume effect. Since the single-pulse temperature increase in the gas is small compared to the average increase, the radial gas profile relaxes to nearly a steady-state value. (Appendix B outlines a simple model for estimating these profiles and the average gas temperature.) Incorporating the full radial and temporal equation Eq. (8) CuRAD calculates the axial gas temperature of the 8-cm laser to be 4200 K, decreasing in a parabolic-like manner to 1600 K at the wall. The electron density in the late afterglow for this laser is in the low 10^{13} cm^{-3} region. Consequently, the electron thermal conductivity is high enough to maintain an almost flat radial electron-temperature profile having a temperature determined by the *average* gas temperature. The electron temperature and average gas temperature is displayed in Fig. 5(c).

There are two macroscopic manifestations of gas-heating effects. The first issue is observed by parameterizing discharge power in a single laser. For a laser of a given diameter and constant wall temperature, as the input power to the laser is increased, laser output power increases until an opti-

TABLE I. Nominal operating parameters for 6–8-cm large-bore CVLs.

	6(cm)	7(cm)	8(cm)
Electrode spacing (cm)	122	122	152
Active length (cm)	90	90	122
Operating temperature (°C)	1500	1450	1450
Neon pressure (Torr)	32	25	25
Copper partial pressure (Torr)	0.3	0.15	0.15
Nominal repetition rate (kHz)	5.0	5.0	5.0
Charge voltage (kV)	14	16.3	18.5
Storage capacitance (nF)	13	12	10.5
Input power density (W/cm^3)	1.85	1.57	1.18
Peak discharge current (A)	1300	1600	2100
Average total power (W)	60	80	100
Code prediction	66	88	115
Light-pulse length (ns)	62	70	85
Code prediction	57	62	75

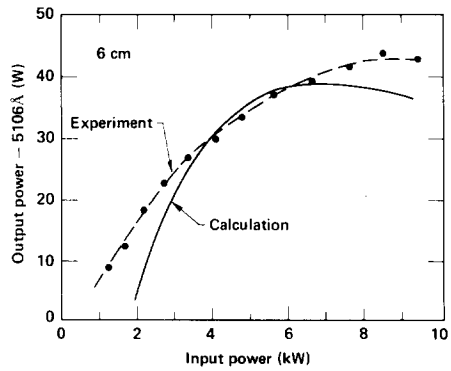

FIG. 6. Laser power (experiment and computed) from a 6-cm oscillator as a function of input power keeping the tube temperature constant. The saturation of laser power is due to an increasingly large fraction of copper atoms in the ^2D level at the beginning of the discharge pulse.

mum power loading is exceeded, after which laser output power begins to fall. The increase in laser power that results from the increased pump rate is offset by an increase in gas temperature and a subsequent increase in the residual, or interpulse, metastable density. In Fig. 6 we see both experimental data and results calculated with CuRAD, confirming this effect for a 6-cm-diam laser. To obtain these experimental data at constant wall temperature, the input power was rapidly varied relative to the thermal time constant of the wall but slowly relative to the thermal time constant of the gas. The good agreement of the code confirms that the saturation in laser power is due to a higher prepulse density of copper atoms in the ^2D level caused by heating of the neon gas.

As one scales to larger laser diameters gas heating effects are manifested by a decrease in optimum power loading as the diameter increases. Table I shows this effect for 6-, 7-, and 8-cm CVLs. For larger-diameter lasers, the more pronounced gas heating at the center of the discharge results in smaller optimum power loading. Calculations have been made for optimum power loading with respect to output power as a function of radius and will be discussed in Sec. IV.

C. Radial behavior

As we move away from the axis of the laser and examine its behavior closer to the walls, we find that as indicated previously the radial dependence of the energy deposition becomes important. Large-bore high-repetition-rate CVL discharges are unusual in that electron densities in excess of 10^{13} cm^{-3} exist under steady-state conditions [see Fig. 5(c)]. As a consequence of the conductivity ($\sim 1.50\,\Omega^{-1}$ cm^{-1}) of these discharges, the skin depth associated with the penetration of the applied electric field can be nearly equal to the diameter of the discharge tube. The penetration of the electric field into the plasma results in a radially dependent time-varying excitation of the gas, which becomes more pronounced as the CVL diameter is increased. As we will show, this effect smooths the radial energy deposition profile, thereby allowing large discharge diameters to be thermally stable.

The reader is referred to Appendix A for a derivation of the skin-depth parameter δ for the penetration of the applied electric field into the plasma. The depth is found to be about 3 cm for our conditions, with a characteristic penetration time of $\tau \approx 2.7\,R^2$ ns, where R (cm) is the radius of the discharge. For discharges less than a few centimeters ($\delta > R$), the longitudinal electric field as a function of radius is nearly uniform. For discharge radii greater than a few centimeters ($\delta < R$), the longitudinal electric field becomes a function of radius.

The computed longitudinal electric field as a function of time and radius for 6- and 12-cm-diam discharge tubes is shown in Fig. 7. Recalling the skin depth is about 3 cm, one sees that the electric field is nearly uniform in the 6-cm case, while there is a delay of almost 75 ns for the electric field to penetrate to the axis of the 12-cm tube. Since the electron temperature is proportional to E/N and the steady-state gas density decreases towards the center of the tube, the electron temperature has complicated dependence on time and radius. This is shown in Fig. 8 for the same conditions as the electric field plots. In the 6-cm example, the electron temperature increases first at the walls and later at the center of the tube, but with a time delay of only 15 ns. In the 12-cm example, the electric field gradient is more pronounced resulting in excitation rates that differ significantly across the tube at a given time.

The gas Joule heating rate, $P = JE = \sigma E^2$, is linked to the electric field. Consequently, the radial penetration of the electric field also affects the energy deposition in large diameter lasers. As shown in Fig. 7, the electric fields tend to peak near the wall. This increases the relative amount of energy deposited in the gas near the walls as the discharge diameter increases. As a result, the relatively cool dense gas near the walls receives the most energy deposition. This tends to smooth out the per atom excitation of the gas, providing a mechanism to stabilize the discharge. As illustrated in Fig. 9, taking skin effects into account, as the diameter of the discharge tube increases, energy deposition changes from being peaked at the center of the discharge to being nearly uniform, thereby providing a thermally stable discharge. With-

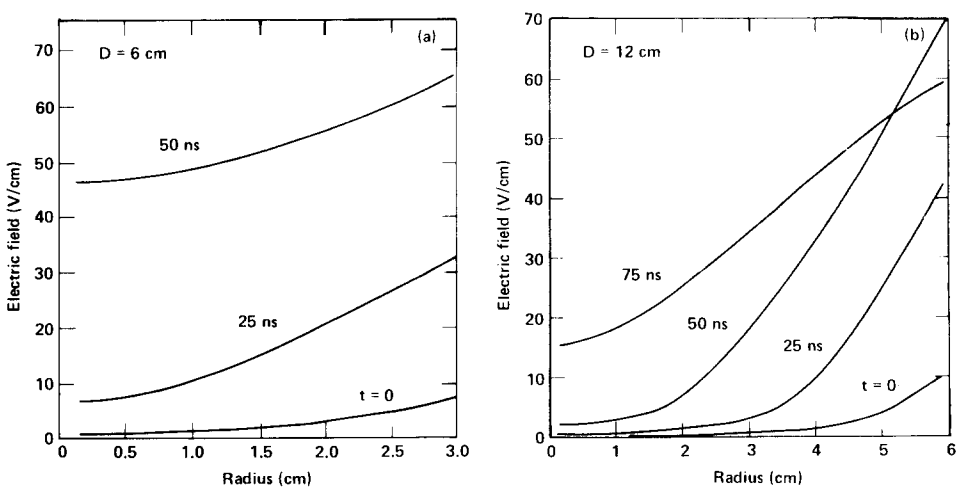

FIG. 7. Computed electric field as a function of radius and time during the discharge pulse for discharge tubes of diameter (a) 6 cm and (b) 12 cm. The electric field is relatively uniform as a function of radius in the smaller tube but has significant gradients due to skin-depth effects in the larger tube. The time $t = 0$ was arbitrarily chosen as the time at which the electric field first appears across the tube.

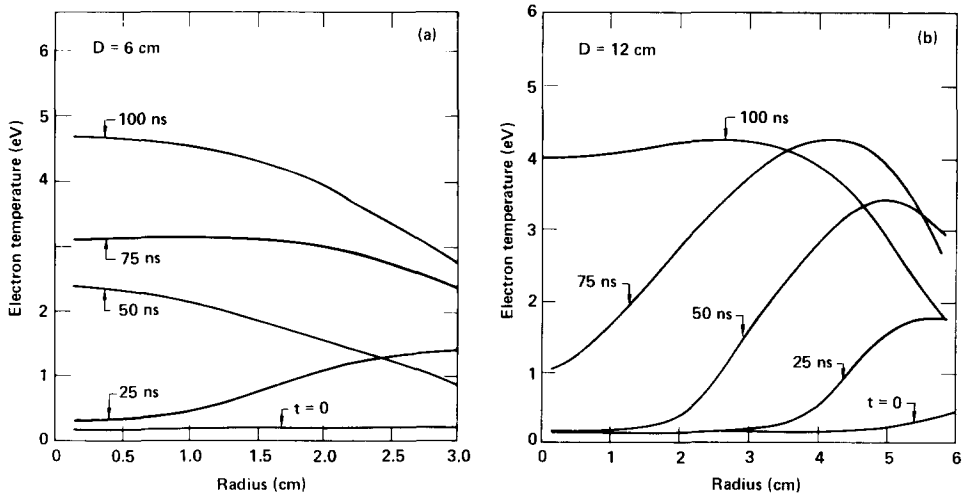

FIG. 8. Computed electron temperature as a function of radius and time for the conditions of Fig. 7 in discharge tubes of diameter (a) 6 cm and (b) 12 cm. Note the severe radial gradients in temperature in the 12-cm case.

out skin effects, the low-density core of the discharge would receive aggressive pumping by the electric field (coupled through the electrons) and quickly overheat, driving the density down even more. This would lead to the familiar thermal instability seen in constricted discharges. Inspection of Fig. 9(b) illustrates this effect by comparing the case of a large-diameter laser with skin effects accurately accounted for and the case where we have deliberately forced the longitudinal electric field to have no radial dependence.

A second consequence of the electric field having to diffuse into the interior of the discharge tube is that excited states of copper and neon are sequentially populated, starting first at the edge of the discharge tube and moving into the center of the tube. Figure 10 presents experimental measurements for the density of the $^2P_{1/2}$ upper laser level as a function of time and radius. The densities were measured using the hook method in a discharge tube 8 cm in diameter. There is a 50-ns delay in the initial excitation of the upper laser level between the wall and the axis. The density at the edge of the tube peaks earlier and falls faster than the center of the tube. Computed results for similar conditions are shown in Fig. 11. The agreement with respect to timing is very good. A delay of 50 ns for the initial excitation is indicated while the peak values have a smaller relative delay. Threshold for laser oscillation occurs at a density that is approximately 30%–50% of the peak value.

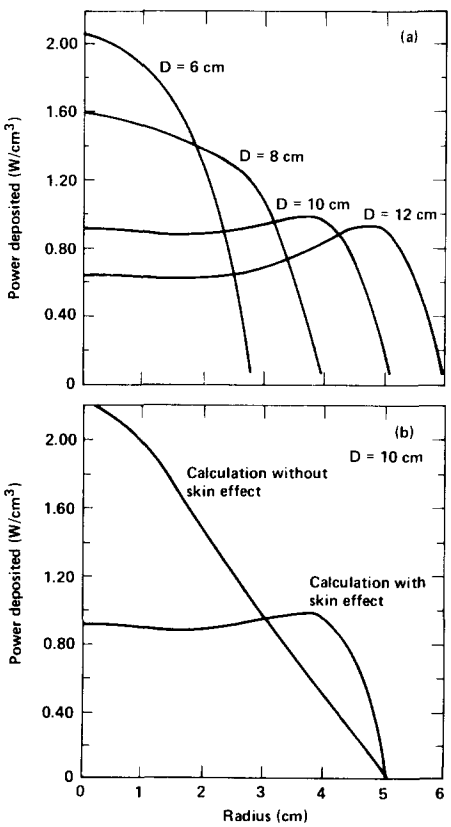

FIG. 9. (a) Radial energy deposition in 6–12-cm-diam CVLs; (b) energy deposition in a 10-cm CVL with and without skin effects (electric field is uniform with respect to radius). Skin-depth effects help maintain uniform deposition.

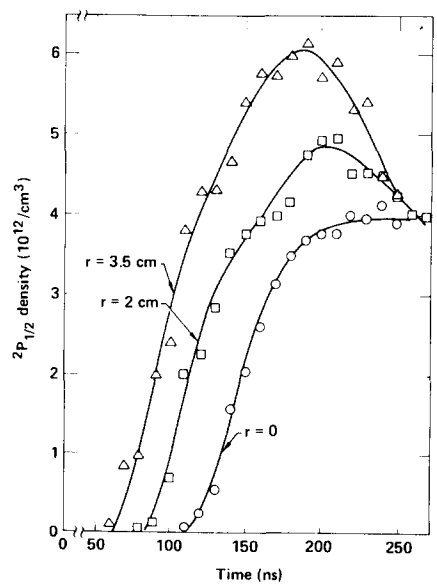

FIG. 10. Hook method spectroscopy density measurements of the $^2P_{1/2}$ (5782 Å) upper laser level as a function of time during the discharge pulse at three radial positions in an 8-cm-diam discharge tube. The delay in excitation between the edge and center of the tube is about 50 ns.

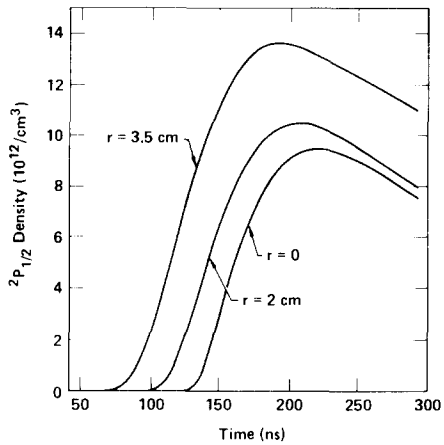

FIG. 11. Computed densities of the $^2P_{1/2}$ (5782 Å) upper laser level, for conditions similar to those of Fig. 10.

The sequential excitation of the laser levels as a function of radius has two important effects on the laser pulse. First, laser threshold is sequentially achieved as a function of radius (assuming a resonator consisting of two flat mirrors). This effect results in the laser pulse initially being annular and changing to a nonannular spot when the inner portion of the tube is excited. Computed laser spot profiles as a function of time in a 12-cm CVL showing this behavior are plotted in Fig. 12.

Experimental and computed results for the time at which the laser pulse turns on as a function of radius in an 8-cm laser are shown in Fig. 13. The excellent agreement confirms that the skin-depth effect accounts for the observed time delays. Note that the time delay for threshold at the center of the tube with respect to a region near the wall is not the same as the time delay required to obtain equal upper-state densities (see Figs. 10 and 11). This is due to the difference in the density of the copper ground and metastable levels and hence the pumping requirements to reach threshold at different radii. For otherwise constant conditions, the absolute density of atoms in the upper level required to reach threshold will be smaller at the center of the tube than the wall, thereby reducing the relative delay. Note also that the differential time delay (change in delay with respect to radius) is smaller near the walls than at the center of the tube. This is a result of the conductivity being lower near the wall, which increases the local diffusion constant for the electric field, thereby decreasing the time required by the local electric field to penetrate into the plasma.

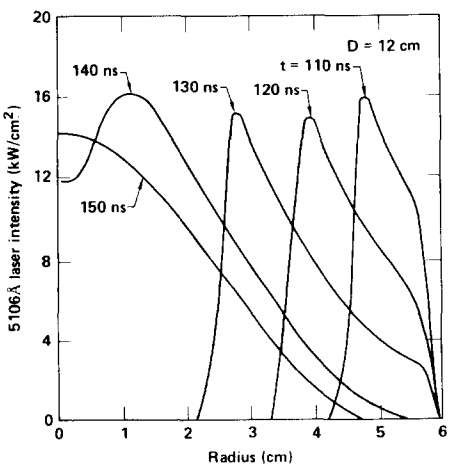

FIG. 12. Laser intensity computed as a function of radius for various times after switch closure in a 12-cm laser where discharge energy has been optimized. Note the radial collapse (in time) of the laser pulse from an annulus to an axial spot.

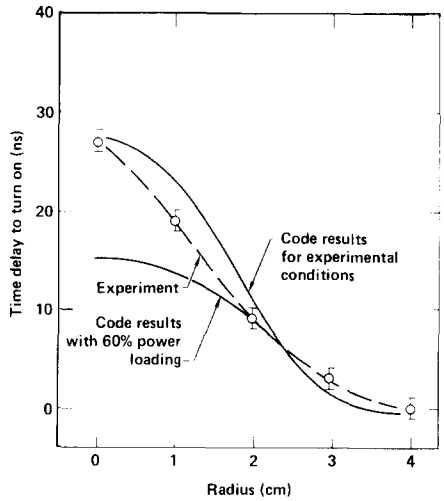

FIG. 13. Experimental measurements and computed values for the time at which the laser pulse turns on as a function of radius in an 8-cm-diam CVL. Also shown are computed results under conditions optimized with respect to input power (power loading about 60% of the experimental conditions).

The second important effect is that the total laser pulse length (integrated over the diameter of the tube) increases as the diameter of the discharge tube increases. This is a result of the sequential excitation of the medium as discussed

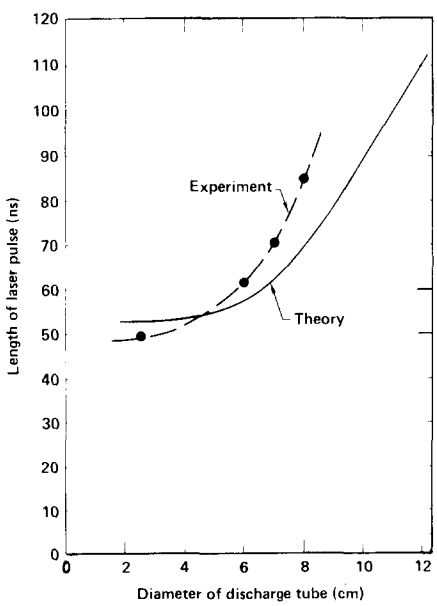

FIG. 14. Experimental and computed values for the total length of the laser pulse as a function of the discharge-tube diameter. Most of the elongation in time of the laser pulse is due to skin-depth effects.

above. In effect, the spatially integrated laser pulse consists of a stack of individual laser pulses coming from annuli with different radii, each delayed by an increment of time. The result is a longer total laser pulse approximately equal to the inversion time plus the penetration time. Computed and experimental results for the total length of the laser pulse as a function of the diameter of the discharge tube are shown in Fig. 14. The agreement is good although the experimental results indicate a somewhat more pronounced effect.

There are two design tradeoffs that will reduce the time delay in excitation from wall to axis. Both involve decreasing the conductivity of the plasma without adversely affecting laser output power. First, by decreasing the average power loading of the laser, the electron density will decrease while the on-axis gas density increases. The resulting decrease in average conductivity can reduce the edge-to-center delay of the laser pulse by as much as 15 ns in an 8-cm laser (see Fig. 13). The decrease in gas heating obtained by decreasing the average power loading has other advantages such as increased electrical efficiency, which will be discussed below.

Secondly, one can also decrease the electron density by dropping the repetition rate and compensating the average power by increasing the discharge pulse energy. The dominant electron-loss mechanism is three-body recombination, which has a rate proportional to $T_e^{-4.5}$ (electron temperature). One can take advantage of this highly nonlinear process by extending the afterglow period (lower repetition rate), giving the electron temperature a chance to decay fully to the gas temperature. This increases both the recombination rate and the time that the electrons have to recombine, yielding lower electron density and smaller light time delays.

IV. SCALING TO LARGER DIAMETERS

In Sec. III we made detailed comparisons between the model and laser operating parameters for devices up to 8-cm diameter. Here, we extend our range of modeling to 12-cm-diam devices and examine their optimization and predicted performance. Calculations with CuRAD on large diameter lasers indicate that laser power can usually be optimized by operating at high charging voltage rather than at high circuit capacitance (see Fig. 15). Since at a given radius the electron temperature must be elevated above a critical value to reach laser threshold, there is a critical electric field that must diffuse into the interior of the tube to reach threshold. As the diameter increases, the applied field (charging voltage) must increase in order for this critical field to be seen on the axis. This consideration leads to increased voltage and smaller storage capacitance to keep the specific energy loading constant as the diameter increases.

The radial gas-temperature profile is a function of the input power density. Clearly, there is an optimum input power density above which thermal effects decrease laser power and below which the laser levels are not sufficiently excited. Due to the increase of thermal effects as the discharge-tube radius increases, the optimum input power density decreases. In the limit of small tubes ($d \leqslant 4$ cm), thermal effects are small since the center of the tube is in good thermal communication with the walls. Maximum laser power is

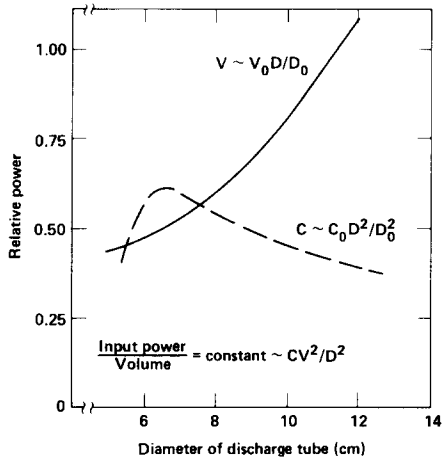

FIG. 15. Computed laser power as a function of discharge-tube diameter where the discharge power per unit volume is constant. The two cases are for increased voltage with increasing diameter (solid line) and increased storage capacitance (dashed line).

obtained in small diameters by pumping as much discharge power into the tube as possible, providing the tube temperature can be specified. The thermal design of the small-bore self-heated CVL need not be efficient.

For large-diameter lasers we try to make the laser highly thermally efficient. This permits the laser to be run at the correct copper density and the optimum power loading. Computed optimum discharge power as a function of diameter is displayed in Fig. 16. The trend towards lower optimum input power as the diameter of the discharge tube increases is clearly shown. A 12-cm laser optimizes at 1/3 the power

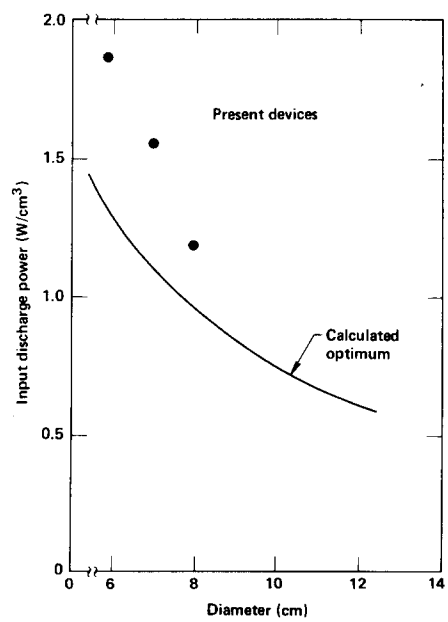

FIG. 16. Discharge power per unit volume optimized with respect to laser power computed as a function of discharge-tube diameter. The actual power deposited in the gas is about two thirds of these values. Also shown is the discharge power per unit volume that is used in present experimental devices.

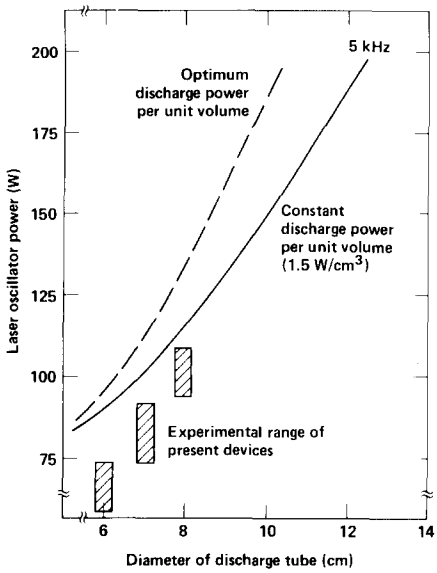

FIG. 17. Computed laser power (oscillator) as a function of discharge-tube diameter. The solid line is for constant discharge power per unit volume (1.5 W/cm^3). The dashed line is laser power optimized with respect to discharge power per unit volume, illustrating the severity of gas-heating effects in the larger lasers. The typical range of output power in present devices is also shown.

density as a 6-cm-diam CVL. Excitation of the large-bore lasers with the optimum input power results in improved average power output and higher efficiency (see Fig. 17). The computed results shown in Fig. 17 are based on 5-kHz repetition rate and increased laser voltage with increased diameter. Two curves are shown: the higher (dashed line) laser output is a result of optimized power loading, while the lower curve (solid line) is for constant input power density (1.5 W/cm^3). (Also shown is the experimental range of data for present 6-, 7-, and 8-cm lasers.) Our code predicts 180 W of output power for a 10-cm-diam CVL and 210 W from a 12-cm device when thermally optimized. Efficiencies are from 1.5% to 2.0%. These performance predictions maintain volumetric scaling of the CVL to 12 cm diameter, a factor of 2 in output over present 8-cm lasers.

Our calculations indicate another benefit to optimized power loading besides the 10%–20% increased output power. The time delay in the light pulse between the outside diameter and the axis is reduced when power loading is optimal. For a 12-cm CVL, light delay time is approximately 80 ns for the 1.5-W/cm^3 case. Decreasing the power loading in this laser to 0.6 W/cm^3 decreases the delay time to approximately 40 ns. (The kinetic origin of this change is discussed in Sec. III.) Figure 12 displays the computed intensity of the 510.6-nm transition as a function of radius and time after switch closure for the 12-cm laser at 0.6 W/cm^3. This behavior is similar to that of our present 8-cm laser in both shape and time dependence.

V. SUMMARY AND CONCLUSIONS

We have developed a comprehensive laser kinetics code that models both spatially and temporally the kinetics of large-bore CVLs. It includes a circuit model, discharge kinetic equations, and specific models for gas-heating and plasma skin effects. We can predict laser-output characteristics of both the yellow and green transitions along with detailed kinetic parameters, including population densities during both the pump pulse and the afterglow of the laser. Predictions of output power for 6-, 7-, and 8-cm devices operating at 5 kHz have shown good agreement with those measured in the laboratory. Both average output power and light pulse length are within 20% with measurements for typical operating regimes. Our confidence in the code CuRAD is particularly high due to the good agreement shown between the hook measurements of copper population densities and the predictions of CuRAD.

The results presented here make it clear that diameter scaling of CVLs can be implemented to provide large single aperture output powers. We believe that we now understand how to achieve the optimal balance between radially dependent energy deposition and radially dependent gas-heating effects. The hook spectroscopy results confirm the radial excitation of the laser transitions and indicate edge to center time delays that are very close to those predicted by CuRAD.

We have found by changing the operating parameters of the laser we can increase or decrease the time delay for the lasing by factors of 2 or 3 in 8-cm-diam lasers. Skin effects are not likely to be seen in smaller CVLs since the penetration time varies as R^2. However, the penetration time is likely to go up for larger high repetition-rate lasers.

Gas-heating effects are found to be important in large-diameter lasers. It is found that the neon temperature on the axis in an 8-cm device is likely to be high as 4500 K and is a cause for the saturation of output power with input power at about the 1.4-W/cm^3 input level. Further increases in input power degrade the efficiency of this laser from its nominal 0.95% value. Scaling lasers to sizes larger than 8 cm is found to require a lower average power loading to somewhat smaller than 1 W/cm^3.

We have used CuRAD to parameterize the output of lasers with 10 and 12 cm diameters and lengths similar to those we now operate. In doing so we found some interesting operating regimes. We found that by dropping the average power loading, increasing the voltage instead of capacitance to increase average power, and running at slightly lower repetition rates, average outputs on the order of 200 W are feasible in 12-cm-diam CVLs.

ACKNOWLEDGMENTS

The authors would like to thank the Copper Laser Development Group at LLNL for excellent technical support, the Theoretical Atomic and Molecular Physics Group for help with cross sections, and E. A. Ault and E. I. Moses for several critical readings of the manuscript.

APPENDIX A: ELECTRIC FIELD PENETRATION DUE TO PLASMA SKIN EFFECT

Here, we estimate the skin depth and associated penetration time of an electric field into a CVL type discharge.[29] We begin with Maxwell's equations:

$$\nabla x\bar{E} + \frac{\partial \bar{B}}{\partial t} = 0\,, \tag{A1}$$

$$\nabla x\bar{B} = \mu_0 \bar{J} + \mu_0 \frac{\partial}{\partial t} \epsilon_0 \bar{E}\,. \tag{A2}$$

By taking the curl of Eq. (A1) and substituting into Eq. (A2) we obtain

$$\nabla(\nabla\cdot\bar{E}) - \nabla^2 E + \mu_0 \frac{\partial \bar{J}}{\partial t} + \mu_0 \frac{\partial^2}{\partial t^2} \epsilon_0 E\,. \tag{A3}$$

Assuming quasineutrality ($\nabla\cdot E = 0$) and dropping the displacement current term [$\partial/\partial t\,(\epsilon_0 E) \ll J = \sigma E$] results in a diffusion-like equation for the longitudinal electric field:

$$\nabla^2 E - \mu_0 \frac{\partial}{\partial t}(\sigma E) = 0\,. \tag{A4}$$

A characteristic skin depth δ for field penetration of an oscillating electric field into a slab is found by assuming a solution of the form

$$E(x,t) = E_0 e^{-x/\delta} e^{i\omega t}\,. \tag{A5}$$

Substituting into Eq. (A4) and solving for δ yields

$$\delta = \left(\frac{2}{\omega \mu_0 \sigma}\right)^{1/2}, \tag{A6}$$

where $\omega = 2\pi f$ is the oscillation frequency of the electric field and the conductivity is

$$\sigma = \frac{e^2 n_e}{m_e \nu_m}\,, \tag{A7}$$

and ν_m is the electron heavy-particle momentum-transfer collision frequency. Just before the excitation pulse in a high-repetition rate 8-cm-diam CVL, $n_e \simeq 2\times 10^{13}$ cm^{-3}. Consequently, $\sigma \simeq 1.5\,\Omega^{-1}$ cm^{-1}. The excitation pulse of the CVL has the characteristic frequency of $f \simeq 2.5\times 10^6$ Hz (200 ns half-sinusoid). These values lead to a skin depth of $\delta = 3$ cm, well within our range of interest. For discharges less than a few centimeters in radius ($\delta > R$), the longitudinal electric field as a function of radius is nearly uniform. For discharge radii greater than a few centimeters ($\delta < R$), the longitudinal electric field becomes a function of radius.

To obtain an estimate for the time required for the electric field to penetrate to the center of the cylindrical discharge, we return to Eq. (A4) and make the assumption that σ is constant during the excitation pulse (accurate within a factor of 2). This results in a diffusion equation for E:

$$D\nabla^2 E - \frac{\partial}{\partial t} E = 0\,, \tag{A8}$$

where the diffusion coefficient is $D = 1/\mu_0\sigma$. Solving Eq. (A8) for cylindrical geometry and radially inward diffusion,[30] the characteristic time for the axial electric field to reach $1/e$ of the applied boundary value is found to be

$$\tau \simeq \frac{0.15R^2}{D} = 0.15R^2 \mu_0 \sigma\,. \tag{A9}$$

Using the quantities discussed above, the time constant for electric-field penetration for an 8-cm CVL is $\tau = 43$ ns. Because of the R^2 dependence of τ, we expect skin-depth effects to become important as the diameter of the laser increases. In CuRAD, skin-depth effects are calculated directly from Eq. (A4), using a temporally and radially dependent conductivity.

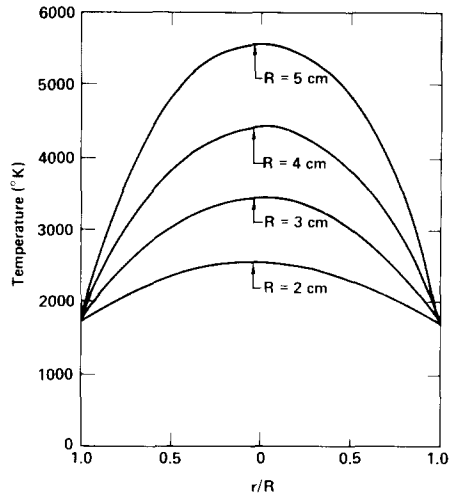

FIG. 18. Gas temperature (neon) as a function of normalized radius (r/R) for various discharge tube radii (R) as calculated with Eq. (B2). The input power deposited per unit volume is constant at 1 W/cm^3 and the wall temperature is 1475 °C.

APPENDIX B: SIMPLE MODEL FOR GAS HEATING

The expected average temperature and profile of the gas can be calculated with certain simplifying assumptions: (1) the average power input is considered uniform in the discharge tube—no radial or longitudinal variations in power density are considered; (2) the wall temperature is assumed to be constant.

The steady-state heat conduction equation has the form

$$\nabla\lambda\nabla T_g = -P\,, \tag{B1}$$

which has the solution

$$T_g(r) = \left[T_w^{m+1} + \frac{P(m+1)}{4\lambda_0}(R^2 - r^2)\right]^{1/(m+1)}. \tag{B2}$$

In Eqs. (B1) and (B2), P is the discharge power deposited in the gas per unit volume, T_w the wall temperature, R the radius of the discharge tube, and the thermal conductivity is $\lambda = \lambda_0 T_g^m$. For neon, $m \simeq 0.5$ and $\lambda_0 = 2.5\times 10^{-5}$ W/cm ^{0}K$^{3/2}$.

For the average power deposited in the gas for our conditions, the temperature can be several thousand degrees. Figure 18 shows the radial temperature profiles for general laser radii as calculated from Eq. (B2) for a constant 1.0 W/cm^3 of power deposited and neon buffer gas (typical large-bore laser pump conditions). Notice that the center gas temperature for an 8-cm-diam CVL rises to approximately 4300 K. The average gas temperature is found by averaging Eq. (B2) over the radius of the discharge tube:

$$\bar{T}_g = \frac{4\lambda_0}{P(m+2)R^2}(T_{g0}^{m+2} - T_w^{m+2})\,, \tag{B3}$$

where the temperature at $r = 0$ is T_{g0} and can be calculated from Eq. (B2).

[1]W. T. Walter, N. Solimene, M. Piltch, and G. Gould, J. Quantum Electron. **QE-2**, 474 (1966).
[2]R. S. Anderson, L. Springer, B. G. Bricks, and T. W. Karras, J. Quantum Electron. **QE-11**, 172 (1975).
[3]I. Smilanski, G. Erez, A. Kerman, and L. A. Levin, Opt. Commun. **30**, 70 (1979).
[4]P. Bokhan, Sov. Phys. Tech. Phys. **26**, 124 (1981).
[5]R. S. Anderson, B. E. Warner, C. Larson, and R. E. Grove, CLEO-81, Digest of Technical Papers, 10–12 June, 1981 (IEEE/OSA), p. 50.
[6]A. A. Isaev and G. Yu. Lemmerman, Sov. J. Quantum Electron. **7**, 799 (1977).
[7]I. Smilanski, A. Kerman, L. A. Levin, and G. Erez, Opt. Commun. **25**, 79 (1978).
[8]P. A. Bokhan, V. I. Silant'ev, and V. I. Solomonov, Sov. J. Quantum Electron. **10**, 724 (1980).
[9]P. A. Bokhan and V. A. Geasimov, Sov. J. Quantum Electron. **9**, 273 (1979).
[10]P. A. Bokhan, V. A. Gerasimov, V. I. Solomonov, and V. B. Shcheglow, Sov. J. Quantum Electron. **8**, 1220 (1978).
[11]V. M. Batenin, I. I. Klimovskii, and L. A. Selezneva, High Temp. **19**, 550 (1981).
[12]M. J. Kushner, J. Quantum Electron. **QE-17**, 1555 (1981).
[13]The equations discussed in this section are solved by calculating spatial derivatives using a fifth-order finite difference technique reducing the system of PDEs to ODEs. By assuming azimuthal symmetry, the boundary condition on the axis is that spatial gradients are zero. Integration of the equations is by a simple first-order Euler method.
[14]R. J. W. Henry (private communication).
[15]A. Z. Msezane and R. J. W. Henry, "Electron Impact Excitation of Atomic Copper," XII International Conference of Physics of Electronic and Atomic Collisions, Gatlinburg, Tennessee 1981, p. 176.
[16]S. Trajmar, W. Wilhams, and S. K. Srivastana, J. Phys. B **10**, 3323 (1977).
[17]N. Winter and A. Hazi, "Review of Electron Impact Excitation Cross Sections for Copper Atom," Lawrence Livermore National Laboratory, Livermore, California, UCID-19314, 1982.
[18]T. Rescigno (private communication).
[19]L. J. Kieffer, "A Compilation of Electron Cross Section Data for Modeling Gas Discharge Lasers," Joint Inst. Lab. Astro. NTIS COM-74-11661, 1973.
[20]W. L. Morgan and L. Vriens, J. Appl. Phys. **51**, 5300 (1980).
[21]M. Mitchner and C. H. Kruger *Partially Ionized Gases* (Wiley-Interscience, New York, 1973).
[22]B. E. Warner and G. V. Seeley (unpublished).
[23]B. E. Warner and M. J. Kushner "Controlling Kinetic Parameters of 100 W Large Bore Copper Vapor Lasers," Proceedings of the International Conference on Lasers '81, Dec. 14–18, 1981, New Orleans, Louisiana.
[24]I. Smilanski, S. E. Moody, B. E. Warner, and J. Flint "Use of Modernized Interferometric Techniques for Laser Diagnostics," Proceedings of the International Conference on Lasers 81, Dec. 14–18, 1981, New Orleans, Louisiana.
[25]I. Smilanski and L. A. Levin, Opt. Lett. **5**, 93 (1980).
[26]B. E. Warner, R. S. Anderson, R. L. Vital, and G. V. Seeley (unpublished).
[27]V. M. Batenin, V. A. Burmakin, P. A. Vokhmin, I. I. Klimovskii, M. A. Lesnoi, and L. A. Selezneva, High Temp. **17**, 975 (1979).
[28]A. N. Soldatov, N. Ya. Shaperev, A. E. Kirilov, V. Ya. Glizer, Yu. P. Polunin and V. F. Fedorov, Sov. Phys. J. **23**, 867 (1980).
[29]S. Ramo, J. R. Whinnery, and T. VanDuzer, *Fields and Waves in Communication Electronics* (Wiley, New York, 1965).
[30]H. S. Carslaw and J. C. Yaeger, *Conduction of Heat in Solids* (Oxford University, Oxford, 1959), p. 233.